Solar Energy 220 (2021) 35–42

Contents lists available at ScienceDirect

Solar Energy

journal homepage: www.elsevier.com/locate/solener

Defects signature in V_{OC} characterization of thin-film solar cells

Atul Kumar [a,*], Pranay Ranjan [b]

[a] ECE Department, KL University, Guntur, Andhra Pradesh 522502, India
[b] Department of Physics, United Arab Emirates University, Al-Ain, United Arab Emirates

ARTICLE INFO

Keywords:
V_{OC}-illumination
V_{OC}-temperature
Bulk defect
SRV
Hole mobility
Contact barrier
Simulation

ABSTRACT

Abnormal features of V_{OC} dependence on temperature and illumination are probed for p-n^{+}-n^{++} heterojunction family of solar cell devices. Thin-film solar cells of CIGS, CZTS, CdTe, SnS have p-n^{+}-n^{++} configuration. V_{OC} plots associated with the device configuration/defect scenarios give identifiable features in a one-sided abrupt heterojunction. These features could be assigned to their generating causes akin to high surface recombination velocity, hole mobility, conduction band offset, resistance, Schottky barrier height and bulk defects. This analysis helps make a general prediction of defects or shortcomings present in the device by observing the V_{OC}-temperature and V_{OC}-illumination plots. An individual defect/shortcoming is introduced at a time in the simulated device model and a comparative study for temperature-V_{OC} and illumination-V_{OC} is performed. Features associated with various device shortcomings (high SRV, hole mobility, conduction band offset, resistance, Schottky barrier height, and bulk defects) are summarized. Finally based on the simulation of V_{OC}-temperature and V_{OC}-illumination plots characterization could diagnose and distinctly identify the defect present in the device.

1. Introduction

Solar cell optoelectrical characteristics like I-V, Q-E, pseudo V_{OC}-J_{SC} plots, temperatures, and illumination dependent performance characterization reveals characteristic insight into device working (Gunawan et al., 2014; Das et al., 2020; Wang et al., 2019; Kumar and Thakur, 2019). A device with defects in the bulk absorber layer or with poorly passivated architecture will show its reflection in these optoelectrical characterizations. Identifying and assigning these reflections to their causes is crucial to mitigate defects and help design high efficiency devices. (Decock et al. 2011, Chen et al. 2021) A thin-film solar cell device due to its heterojunction character is susceptible to interface issues akin to the Schottky barrier at metal contact, dangling bond, lattice mismatch and band offset at p-n interfaces which have repercussions on performance. Presence of bulk defects if any in different layers further compounds the situation. The operational device might have all these together, and their conjunct effect might be observed on electrical characterization. The visible feature in I-V, V_{OC}-Temperature/illumination, C-f, C-V, and QE characteristics are the compound signature of such shortcomings. Fig. 1 shows a schematic of I-V characteristics of the inorganic thin-film solar cell with identifiable signatures that could be assigned to well-known defects (Kumar and Thakur, 2019; Reenen et al., 2015). Curve marked 0 is showing J-V for the ideal device in dark, 1 is showing J-V for the ideal device in light, 2 shows hysteresis behavior, 3 shows an s-kink, 4 suboptimal resistance, 5 roll-over behavior, 6 crossovers in J-V. Similarly, bulk shallow defect N1 existing in CIGS as observed by admittance characterization (Krysztopa et al., 2013). The practical device may have different defects and architectural shortcomings present in various combinations simultaneously. Thus, a signal from such a device contains convoluted information that is implicit to precisely resolve. The task becomes complex when interpreting and distinctly assigning the signature to a particular defect. A one-to-one relation of features and controlling parameters not only provides an insight into the device working but also enable faults finding in experimental devices. Experimental solar cell with lower efficiency requires extensive characterization for determining the root cause of their performance limitation. This is a challenging and cost-intensive process. Simulation study aimed at identifiable abnormal features could assist in the study of shortcomings in the device. We here present the simulation-based study for establishing one to one relation of features and controlling parameters in thin-film solar cell devices. The solar cell performance parameters (Efficiency, V_{OC}, J_{SC}, FF) are dependent on the device specification and architecture. The relation between performance parameters on the device specification is shown comprehensively in Fig. 2.

We first simulated a thin-film solar cell with high efficiency of 20%

* Corresponding author.
E-mail address: atul.pph14@iitp.ac.in (A. Kumar).

https://doi.org/10.1016/j.solener.2021.03.017
Received 26 September 2020; Received in revised form 27 February 2021; Accepted 7 March 2021
Available online 25 March 2021

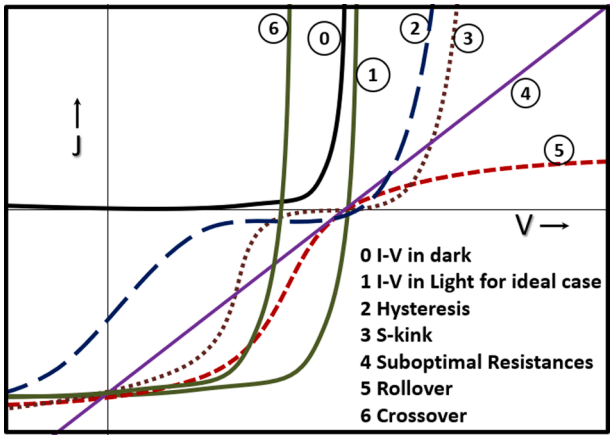

Fig. 1. The Schematic of J-V curve based on the (Kumar et al. 2000) depicting the ideal, hysteresis, S-kink, resistance, rollover, crossover signature as marked from 1 to 6 in J-V curve. All these features in J-V curve could be distinctly assigned to a particular defect scenario in the device.

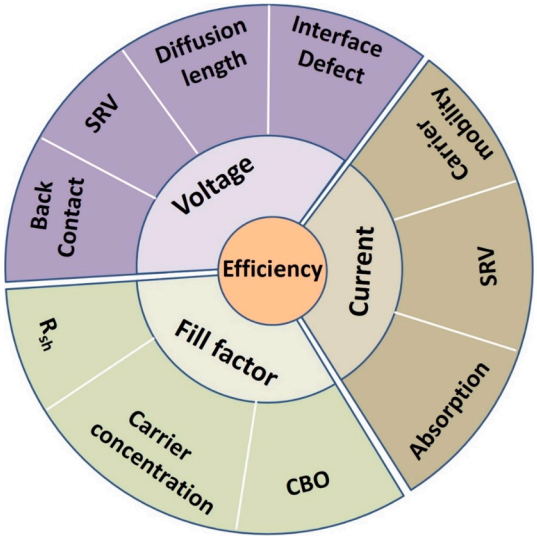

Fig. 2. The schematic showing the hierarchal inter-relation of the design criterion on performance parameters (V_{OC}, J_{SC}, FF) and efficiency.

(corresponding to CdTe thin-film devices). The efficiency is matched to the experimental device in terms of performance and device parameters in Section 2. The signature feature related to defect density, defect energy level, back contact barrier, resistance, hole mobility, surface recombination velocity, and conduction band offsets in temperature and illumination dependent V_{OC} curves are identified and summarized in Section 3.

2. Simulation details

The insight into the signature effect of various defects on electrical characteristics is generated using a 1D solar cell simulation package SCAPS-1D (Solar cell capacitance simulator) version 3.3.02. SCAPS-1D is developed by the University of Gent researchers (Burgelman et al., 2000). SCAPS solves basic 1D drift–diffusion and continuity eq. to numerically simulate I(V), C(V), and C(f), Quantum efficiency curve, band diagram, recombination across *p–n* heterojunctions structures. The system of semiconductor equations from 1 to 5 are solved in the one-dimensional format in SCAPS. Across the interface and bulk of the layers, these equations are solved with the constitutive equations. The heretosystem of these equations is solved numerically, using a Gummel

Table 1
The device configuration and corresponding material parameters as utilized in simulation.

Parameters	*p*	*N*	n^{++}
Thickness (μm)	0.6	0.05	0.5
Bandgap (eV) (E_g)	1.5	3	3
Electron affinity (eV) (χ)	4.5	4.4	4.55
Dielectric permittivity (ε)	10	10	9
Electron/Hole thermal velocity (V^e_{th})/ (V^p_{th}) (cm/s)	10^7	10^7	10^7
Electron/hole mobility (cm^2/Vs) (μ_e)/ (μ_h)	50	50	50
Donor/Acceptor density, N_D /N_A (cm^{-3})	10^{16}	10^{18}	10^{19}
Absorption coefficient (cm^{-1})	10^5	SCAPS file	SCAPS file
Bulk defect density (cm^{-3}) varied (10^{13}-10^{17})			
Defect energy level (eV above E_V) varied (0–0.75)			
Work function of back contact (eV) varied			
R_{Sh}, R_S (Ωcm^2) varied (800, 2)			
Surface recombination velocity electron/hole (cm/s) varied (10^2-10^7)			
Hole mobility (cm^2/Vs) varied			
Conduction band offset (eV) varied (-0.1, 0.1, 0.3)			

iteration scheme with Newton-Raphson substeps. Using appropriate boundary conditions at the hetro-interfaces and various contacts, it solves the coupled differential equations in (Ψ, n, p) or (Ψ, E_{Fn}, E_{Fp}). SCAPS numerically calculates a steady-state and a small signal solution of this system. Heretostructure is first discretized by creating a mesh and a steady-state working point is achieved using a small-signal analysis.

$$J_n = -\frac{\mu_n n}{q}\frac{dE_{Fn}}{dx} \tag{1}$$

$$J_p = \frac{\mu_p p}{q}\frac{dE_{Fp}}{dx} \tag{2}$$

$$-\frac{dJ_n}{dx} - U_n + G = \frac{dn}{dt} \tag{3}$$

$$-\frac{dJ_p}{dx} - U_p + G = \frac{dp}{dt} \tag{4}$$

$$\frac{d}{dx}\left(\varepsilon_0\varepsilon_r\frac{d\Psi}{dx}\right) = -q(p - n + N_D^+ - N_A^- + \frac{\rho_{def}}{q}) \tag{5}$$

where the symbols have the usual meaning (SCAPS Manual). It can optimize solar cell device configuration (Burgelman et al. 2000, Meher et al. 2016, Islam and Thakur, 2020, Sadanand, 2019, Kumar, 2021a), simulating light soaking (Kumar and Ranjan, 2020), crossover, rollover, skink, impurity photovoltaic effect, multijunction, tunneling effect, hysteresis (Kumar, 2021b) and other phenomena related to PV devices using special conditions, defect models, script file, batch setup, etc. Thus the effects of absorption, inter and intra band tunneling, defects energy level, and recombination can also be graphically illustrated by this software package in thin film solar cells. For detail of SCAPS reader can have a look on the literature (Kumar and Thakur, 2018a; Kumar and Thakur, 2018b; Kumar and Thakur, 2018c; Kumar and Thakur, 2018d; Kumar and Ranjan, 2018e).

The present simulation study reveals that certain uncommon characteristic feature in electrical characterization which could be assigned to dominating scenario in device structure or configuration. For example, shunt resistance decreases the fill factor, which could be visualized in the I-V curve (Kumar and Thakur, 2019). The impact of bulk defect density, defect energy level in the forbidden gap, hole mobility within absorber, resistance, temperature, surface recombination velocity at contact, back contacts and conduction band offset are brought out in V_{OC} illumination and temperatures curve. The improper values of these parameters in the device designing/device configuration not only lower device performance but also leave an identifiable signature on electrical curves. For this, we have simulated a standard CdTe solar cell with an efficiency of 20%. The simplified CdTe device

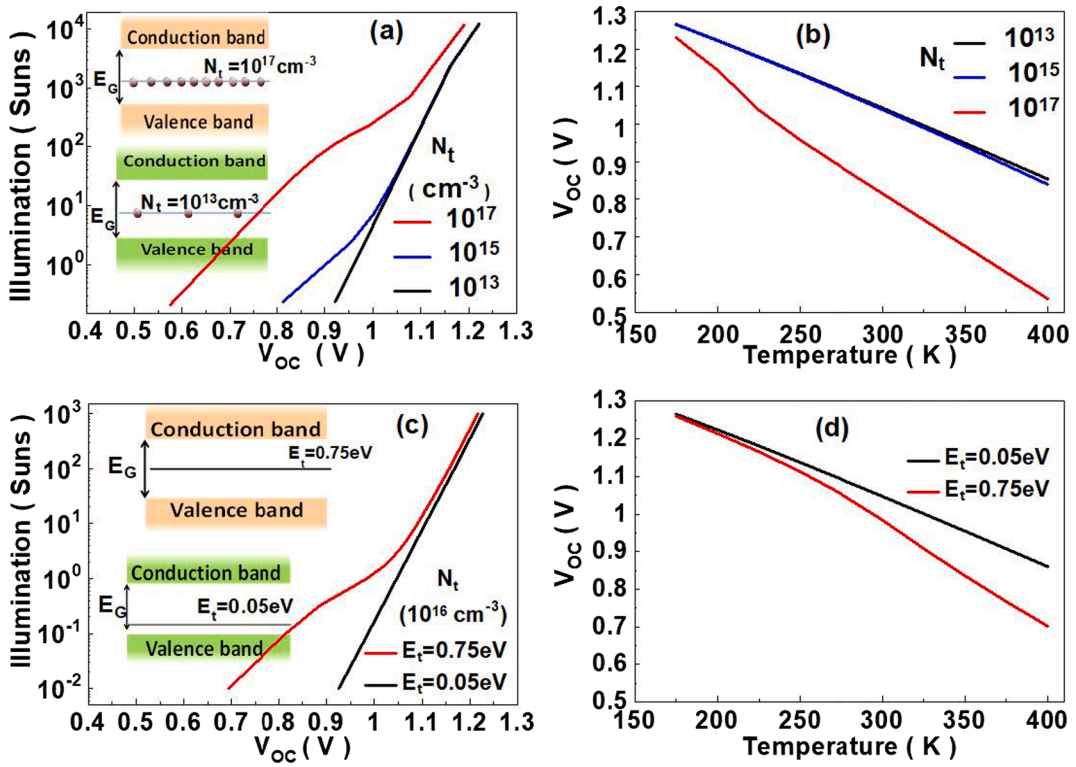

Fig. 3. (a) The V_{OC}-illumination simulation for bulk defect density variation in the absorber. The recombination mechanism is dependent on defect density. For low defect density, the dominant recombination mechanism is band to band. For high defect density, SRH and Auger recombination are dominating recombination mechanism. At higher illumination the generation rate is overcoming this carrier density mediate SRH recombination, thus V_{OC} recovers up as shown by simulation. (b) V_{OC} as a function of temperature is plotted for various defect densities. As the temperature decreases V_{OC} followed a linear increasing slope. For higher defect density this slope becomes nonlinear as carrier density dependent SRH and Auger recombination is pronounced at high temperature. These recombination process decreases at a lower temperature, thus as shown in the simulation. (c) V_{OC}–illumination simulation for defect energy levels variation in the forbidden gap of the absorber. V_{OC} is sensitive to low illumination intensity and this sensitivity increases for mid-gap defect level. (d) V_{OC}-temperature simulation reveals the lowering of V_{OC} in presence of mid-gap defects at higher temperatures.

structure consisting of three layers: standard CdTe absorber (*p*-type) layer, CdS buffer, and highly doped ZnO window. In the exact device configuration is CdTe/CdS/i-ZnO/ZnO:Al, a p-n^{+}-n^{++} configuration. The material parameters are appropriately taken from experimental devices as reported in the literature and agree with reported devices (Metzger et al., 2019; https://www.greentechmedia.com). The reasonable values of the parameters of CdTe absorber and buffer layer were collated from literature and are listed in Table 1. Acceptor and donor densities, relative permittivity, electron affinity, E_g the bandgap energy value, mobility of electron, and hole are very well known for CdTe. Carrier type and density of the absorber, which are one of the most important parameters, are assumed to be p-type and 10^{16}cm^3. N_t (bulk defect density) for the absorber was varied 10^{13}-10^{17} cm^3 to adjust the carrier diffusion lengths of electrons and holes. The conduction band offset between buffer/absorber layers is varied in the range of −0.3 to 0.3 eV by adjusting the electron affinity of the buffer layer. The impact of band offsets among buffer, absorber, and interface is simulated in dark I-V. Absorption pre-factor for absorber layer A_α is assumed to be $\sim 10^5$ to obtain absorption coefficient (α) curve calculated by $\alpha = A_\alpha(h\nu\text{-}E_g)^{1/2}$, where the hν is the photon energy. Also, the carrier diffusion length of the CdTe is set at 1 μm, corresponding to the experimental carrier diffusion length in a range of 1.07–1.21 μm. E_t (defect energy level) is located at the centre of E_g and distributed in Gaussian with a characteristic energy of 0.1 eV, and the defect type is neutral. This high bandgap, the thin-film device is chosen for simulation to reveal the abnormal I-V characteristics and their origins. In a device, it might so happen that multiple deficiencies are present and modulate electrical characteristics simultaneously. To evaluate this, we first need to identify the individual impact of shortcomings on electrical characteristics. For this high efficiency (>20%) device various scenarios are simulated in the device and the corresponding signature is revealed in the Illumination-V_{OC} curve, Temperature-V_{OC} curve and dark I-V curves.

3. Results and discussion

Open circuit voltage V_{OC} is a sensitive output parameter, affected by defects and recombination mechanisms in a photovoltaic device. Under different defect scenarios, the V_{OC} dependence on illumination and temperature could reveal the underlying recombination mechanism and identify the defect responsible. V_{oc} increases with increasing illumination intensity and is given empirically as $V_{oc} = V_{oc}^{'} + \frac{nKT}{q} lnX$, where X is the suns intensity. V_{OC} is highly dependent on temperature through saturation current J_0 which is dependent upon temperature given by $J_o = CT^3 e^{-\frac{E_G}{KT}}$, where C is a constant. As temperature increases J_0 increases thus V_{OC} decreases with increasing temperature, $V_{oc} = \frac{kT}{q}\ln(\frac{J_{SC}}{J_0} + 1)$. The dependence of V_{OC} on temperature is given mathematically (Singh and Ravindra, 2012) as

$$\frac{dV_{oc}}{dT} = \frac{V_{oc}}{T} + \frac{nKT}{q}\left(\frac{1}{J_{SC}}\frac{dJ_{SC}}{dT} - \frac{1}{J_0}\frac{dJ_0}{dT}\right) \quad (6)$$

The absorption of photons generates a transient hole and electron density in the valence and conduction band respectively. Thus, the voltage is given by $V_{oc} = \frac{E_{Fn} - E_{Fp}}{q}$, (Elumalai and Uddin, 2016) where E_{fn} and E_{fp} are the quasi-Fermi levels under illumination. Any leakage path will reduce this transient hole and electron density buildup i.e. $E_{Fn} - E_{Fp}$ and thus the voltage output. The leakage path may be mid gap state causing recombination within the bulk. Bulk defect energy level in

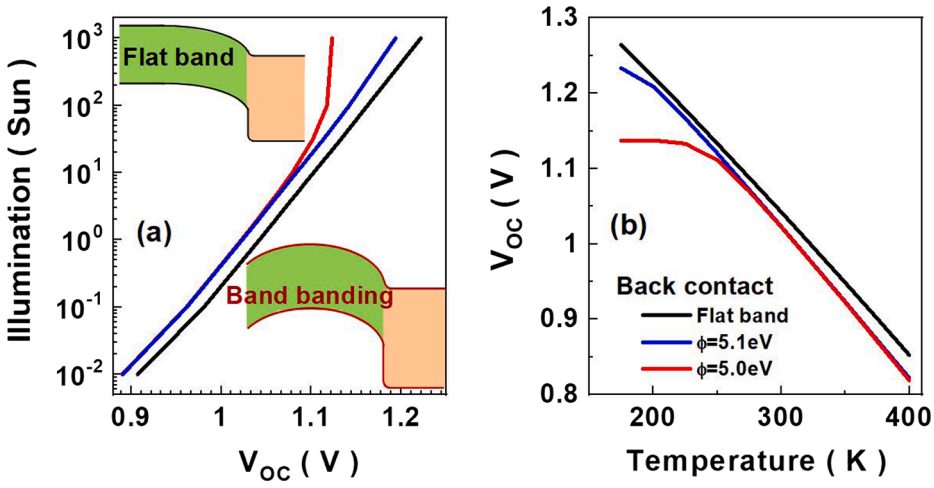

Fig. 4. (a) V_{OC}–illumination simulation for the scenarios of the flat band and back contact barrier in the device. A schematic of the band diagram of the flat band and band bending due to the back contact barrier is shown in the inset of figure (a). V_{OC} saturates for increasing back contact barrier. (b) V_{OC} versus temperature plot for increasing back contact barrier height shows open circuit voltage saturation at lower temperatures for a low work function of back contact.

the forbidden gap will cause SRH recombination. V_{OC} decrease with the defect density and defect energy level approaching the midgap state in the forbidden gap. The bulk defect increase will decrease in diffusion length, diffusion coefficient, built-in voltage, as given by, (Rau and Schock, 1999)

$$V_{oc} = \frac{E_g}{q} - \frac{2KT}{q}\ln\left(\frac{kTD_n\pi\sqrt{N_C N_V}}{J_{sc}L_D^2\sqrt{2qN_A V_{bm}/\varepsilon}}\right) \tag{7}$$

where $2KT/q$ is the thermal voltage, D_n the diffusion constant for electrons, $N_{C/V}$ the effective density of states in the conductance/valence band, N_A the acceptor density, and L_D the diffusion length. The V_{OC} dependence on lifetime is given by (Luque and Hegedus, 2003)

$$V_{oc} = \frac{2kT}{q}\ln\left(\frac{G_L\tau_0}{n_i}\right) \tag{8}$$

where G_L is the generation rate, n_i is the intrinsic density, τ_0 is the lifetime. The lower lifetime in device lowers the V_{OC} output. Schottky barrier height limits the V_{OC} output severely and has slope changes for higher barrier height as compared to flatband. As the barrier height increase, the voltage is limited severely as given by (Rau and Schock, 1999) $V_{oc} = \frac{E_a}{q} - \frac{nKT}{q}\ln\left(\frac{J_{00}}{J_L}\right)$ where diode ideality factor (n), E_a is the activation energy, diode saturation current (J_{oo}) is dependent on the device recombination process. J_{oo} is given by $J_o = J_{00}\exp\left(\frac{E_a}{AkT}\right)$

3.1. Impact of bulk defect density

The variation of V_{OC} under varied illumination intensity for a 20% efficient solar cell is simulated. A high-efficiency device is chosen so that the individual impact of defect could be shown. V_{OC} rises linearly with increasing illumination intensity for the defect-less case. V_{OC} reduces at low illumination in the case when we increased defect density as shown in Fig. 3. With increasing defect density, it is observed that the V_{OC} is reduced in low illuminations region. Even though the trends of V_{OC} increment with the illumination is maintained. At low illumination, V_{OC} reduction is pronounced. A scenario of three defect densities is simulated, for low defect density in absorber (10^{13} cm^{-3}) the dependence is a straight line with a constant slope. For intermediate defect density, (10^{15} cm^{-3}) V_{OC} reduction at lower illumination is visible. For higher illumination, the curve overlaps the curve of lower defect density. For the case of high defect density 10^{17} cm^{-3}, there is a lowering of V_{OC} for all illumination ranges however this lowering is pronounced at the lower illumination region. At low defect density, the dominant recombination mechanism is band to band recombination. For higher defect density, the dominant recombination mechanisms are SRH and Auger recombination. The carrier density dependence of theses various recombination mechanism is shown empirically in equation (9). (Tress et al., 2018)

$$R \approx \begin{cases} np\beta band\ \ to\ \ band\ \ recombination \\ \dfrac{np}{\tau_p n + \tau_n p} SRH\ \ recombination \\ cn^2 pAuger\ \ recombination \end{cases} \tag{9}$$

The V_{OC} is lower for high defect density and V_{OC} recovers for high illumination intensity. V_{OC} is given by following mathematical eq for band-to-band recombination and SRH recombination

$$qV_{OCb2b} = E_g - K_B T ln\frac{N_C N_V \beta}{G} \tag{10}$$

$$qV_{OCSRH} = E_g - K_B T ln\frac{N_C N_V}{N_D \tau_p G} \tag{11}$$

V_{OC} as a function of temperature for varied defect density in the absorber is simulated in Fig. 3b. The V_{OC} increases linearly with decreasing temperature for the case of low defect density as shown. For high defect density V_{OC}-temp. slope increases. It is observed that the lower temperature the effect of defect density in the absorber layer on V_{OC} is minimal. We have performed simulations up to 175 K only as simulations below 175 K are giving convergence failure. At higher temperature region the recombination rate is high thus V_{OC} significantly vary for different defect densities. At lower temperature the recombination reduce significantly, thus V_{OC} become almost same for different defect densities. The presence of defect energy level near to band edge (0.5 eV above valence band edge) does not reduce V_{OC}. The midgap defect level severely lowers the V_{OC} in the lower illumination region (below one sun). V_{OC} falls steeply with lower intensity for the mid-gap defect. For temperature dependence, in a higher temperature region, the effect of the mid-gap defect in reducing the V_{OC} is prominent. Seeing from the above simulation in Fig. 3(a-d), it concluded that the defect density has a severe impact on V_{OC} output. V_{OC} severely decreased in the low illumination intensity region and high temperature region in presence of high defect density. The impact of high defect density is nullified in the high illumination and low temperature region.

3.2. Impact of back contact

The back-contact barrier in the device causes crossover in thin-film

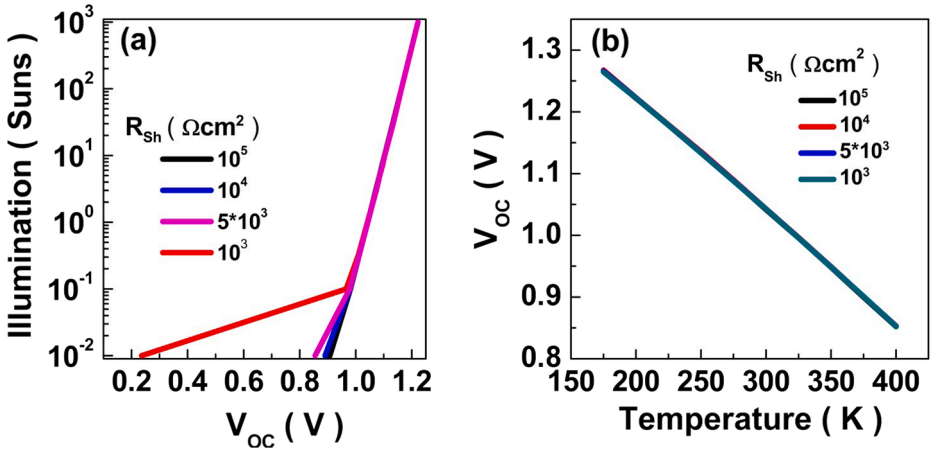

Fig. 5. (a) The V_{OC}-illumination simulation for shunt resistant variation. V_{OC} shows a steep decrease at lower illuminations intensities for low shunt resistance. (b) V_{OC} vs temperature plot for different shunt resistance values. The curve is linear and overlapping irrespective of the resistance values.

solar cell devices and limits V_{OC} output. The schematic of the ideal case of the flat band and a band bending due to contact barrier at the rear metal contact in the device as shown in Fig. 4(a). Work function (Φ) of contact metal should be higher than electron affinity (EA) and bandgap (E_G) of absorber combined for the flat band condition ie $\Phi >= EA + E_G$. Undesired band bending at the back contact occurs for the condition $\Phi < EA + E_G$. Such underside and detrimental contact barrier are present due to a non-ohmic contact with the *p*-type absorber layer. Generally, conductive metals have a low work function (Φ, less than 5 eV). This makes it difficult to form an ohmic contact with a p-type absorber with bandgap E_G 1.5ev and electron affinity 4 eV. The identifiable feature associated with such contact barrier is simulated in the V_{OC}-illumination and V_{OC}-temperature plot in Fig. 4(a-b). V_{OC} illumination shows that in presence of back contact in the device, voltage initially increases with illumination at lower intensities and becomes independent of illumination intensity at the higher illumination levels. The Schottky barrier is aligned opposite to the *p-n* junction in the device (Green et al., 1990; Gunawan et al. 2010). Voltage drop V_{back} across the back contact Schottky barrier is opposite to that induced by the forward bias ie voltage at the *p-n* junction $V_{p\text{-}n}$. This negative voltage drop adds to the $V_{p\text{-}n}$ such that the net output voltage is given by junction voltage $V_{output} = V_{p\text{-}n} - V_{back}$ (Pan et al., 2006). The *p-n* diode voltage $V_{p\text{-}n}$ increases with illumination intensity. At the same time Schottky voltage V_{back} also increase with illumination intensity. This causes the net output voltage saturation at high illuminations. Temperature dependence of voltage shows V_{OC} saturation for back contact barrier at a temperature lower than 250 K. The lower temperature decreases the dark reverse saturation current of Schottky barrier (given by Eq. (12)). Thus, net V_{OC} saturates at low temperatures for high barrier. The Shockley diode equation and the thermionic emission Schottky diode equation are given by (Kaushal et al. 2012).

$$I_{Schockley} = I_L - I_0\left(e^{\frac{qV}{nKT}} - 1\right) - \frac{V}{R_{SH}}; \quad I_{Schottky} = I_0^* exp^{\left[-\frac{q\varphi_B}{KT}\right]}\left(exp^{\frac{qV}{nKT}} - 1\right) \tag{12}$$

Also the φ_B metal semiconductor barrier height has a negative temperature gradient. The effective barrier height is given by $\varphi_{Beff} = \varphi_B - \alpha T$ where α is the negative temperature coefficient of the barrier height. (Altındal et al. 2007) Thus at lower temperature V_{OC}-temperature plot shows saturation. This behavior is distinct from the V_{OC}-illumination in presence of bulk defects. The saturation of V_{OC} at higher illumination intensities could be distinctly assigned to back contact barrier issues present in devices. The presence of a back-contact issue in the device could be ascertained in solar cell devices by performing the V_{OC}-illumination and temperature characterization.

3.3. Impact of resistance

The impact of resistance on the solar cell is marked by the decrease in FF values. The relation between FF and shunt resistance is given by (Martin A Green, 1982)

$$FF_{sh} = FF_o\left(1 - \frac{v_{oc} + 0.7}{v_{oc}}\frac{FF_o}{r_{sh}}\right) \tag{13}$$

where FF_0 is the ideal FF in the absence of series resistance, r_{sh} is the shunt resistance normalized to the cell's characteristic resistance. This impact of resistance causes a distinct feature in I-V curve as shown by 4 in Fig. 1 (Kumar and Thakur, 2019). The shunt resistance R_{SH} dependence of voltage is given by Shockley Eq. (12) which is rewritten as

$$V = \frac{nKT}{q}\ln\frac{I_L - I - \frac{V}{R_{SH}}}{I_o} \tag{14}$$

The impact of suboptimal resistance values in the device is simulated in Fig. 5. Shunt resistance signifies the internal recombination in the device. V_{OC}-illumination characterization provides a signature of shunt resistance in devices. In low illumination region with an intensity lower than <0.1 suns, V_{OC} is observed to be decreasing steeply for lower shunt resistance. It shows high internal recombination for low conductivity in low illumination intensity. The temperature dependence V_{OC} increases with lowering temperature, as at lower temperature the internal recombination will cease/reduces. For low shunt resistance, the deteriorating shunt resistance is counter balance by reduced recombination thus there is no saturation observed in V_{OC}-temp. The dependence of V_{OC} on resistance R_{SH} is given by Eq. (15). The V_{OC}-temperature curve is linear and overlapping for different shunt resistance values. There is no detrimental impact of shunt resistances. Taking these two curves V_{OC}-illumination and V_{OC}-temperature, it can be said that the shunt resistance causes a characteristic V_{OC} loss in the lower illumination region and no change in temperature plots. In case of SRH defect, internal recombination is dependent on carrier concentration, whereas low conductivity caused recombination is independent of carrier concentration. The V_{OC} decreases at higher temperature is absent for the shunt resistance case. The combined temperature and illumination plots give distinct features from that of the bulk defect caused recombination as shown in Figs. 3 and 4.

3.4. Impact of the mobility of hole mobility

Absorber material has carrier mobility from 0.05 to 1 cm^2/Vs. The performance of devices depends upon carrier mobility as can be seen in silicon, perovskite (Würfel et al., 2015; Kaienburg et al., 2020). Carrier

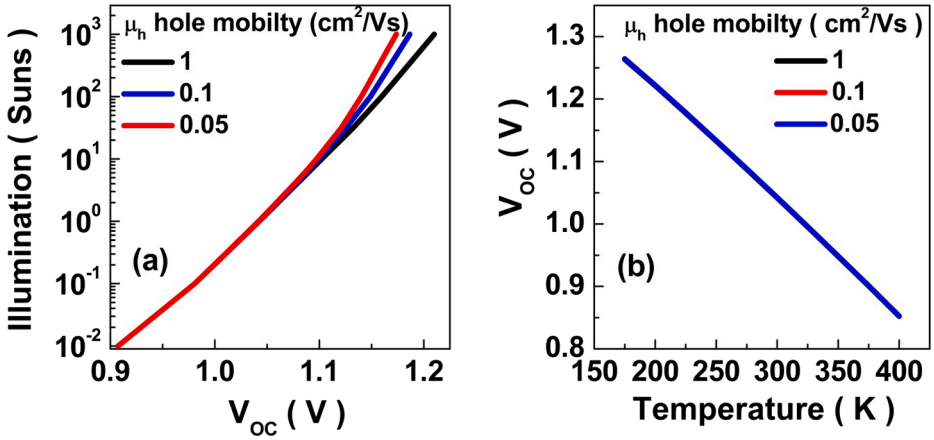

Fig. 6. (a) The V_{OC}-illumination simulation for increasing hole mobility values. V_{OC} does not show any variation at lower illumination intensity irrespective of hole mobility values. V_{OC} saturates at higher illumination intensities for lower hole mobilities. (b) V_{OC} linearly increases with temperature and is independent of hole mobilities.

mobility has an impact on device performance, mobilities below 1 cm^2/Vs are detrimental for higher efficiency. The impact of hole mobility on V_{OC} is simulated in Fig. 6. The V_{OC} linearly increasing for all mobilities (higher than 0.05 cm^2/Vs) at the lower illumination region as shown in Fig. 6(a). However, lower mobility in devices causes V_{OC} limiting effect at the higher illumination intensities. The saturation of V_{OC} due to lower mobility at a higher intensity is moderate as compared to saturation caused by the contact barrier.

The hole current is given by

$$J_p = qp\mu_p E \tag{15}$$

where E is the electric field, μ_p is hole mobility. When μ_p is 1 the electric field required is 1, when μ_p is 0.01, the required E electric field is 100 to maintain the same current J_p. The electric field required at lower mobility is high which cause the band bending at the hole junction. High illumination intensity will generate high density of hole. The bending near the rear junction is caused due to the failure of the hole extraction from this region. This undesirable condition cause V_{OC} pinning and voltage drop in the back region. The saturation of V_{OC} increases with decreasing mobility at higher illumination concentration in the absorber. The temperature-dependent V_{OC} has linear and overlapping curves for different hole mobilities as shown in Fig. 6(b). At low temperature recombination process reduces which counterbalance the band banding due to hole accumulation at back. Thus, here is no net effect on V_{OC} under temperature variation. The combined temperature and illumination dependence of V_{OC} for varied hole mobility showed distinct curves, different from that observed in bulk defect, contact barrier, and resistances cases.

3.5. Impact of surface recombination velocity

The surface recombination velocity (SRV) corresponds to minority carrier lifetime in bulk semiconductor, and could be given by SRV = $R_s/\Delta n_s$, where R_s is surface recombination rate, Δn_s is excess minority carrier concentration at the surface (Wang et al., 2019). SRV impact the effective lifetime as given by (Sproul, 1994)

$$\tau_S = \frac{W}{2S} + \frac{1}{D}\left(\frac{W}{\pi}\right)^2 ; \frac{1}{\tau_{eff}} = \frac{1}{\tau_b} + \frac{1}{\tau_S} \tag{16}$$

where W is layer thickness, D is carrier diffusivity, S is SRV, τ_{eff} is the effective lifetime of carriers. The V_{OC} is directly proportional to the effective lifetime as given by equation (8). Thus, lower SRV gives optimal open circuit voltage. Low SRV values are obtained by passivated contact and result in higher device performance. We ran simulations utilizing SRV values from 10^2-10^5 cm/s in high-efficiency CdTe devices. V_{OC} is directly proportional to the effective lifetime. High SRV lower the effective life time as given by Eq. (17). There is a dc shift decrease in open circuit voltage values for high SRV values as shown in Fig. 7(a). V_{OC} increases linearly with increasing illumination intensity for various SRV. The schematic for SRV impact on devices is shown in the inset of Fig. 7(a). Temperatures dependent V_{OC} shows a linear rise with decreasing temperature. V_{OC}-Temp remain constant slope because high SRV values are counter balance by reduced recombination with decreasing temperature. The simulation shows that lower SRV values

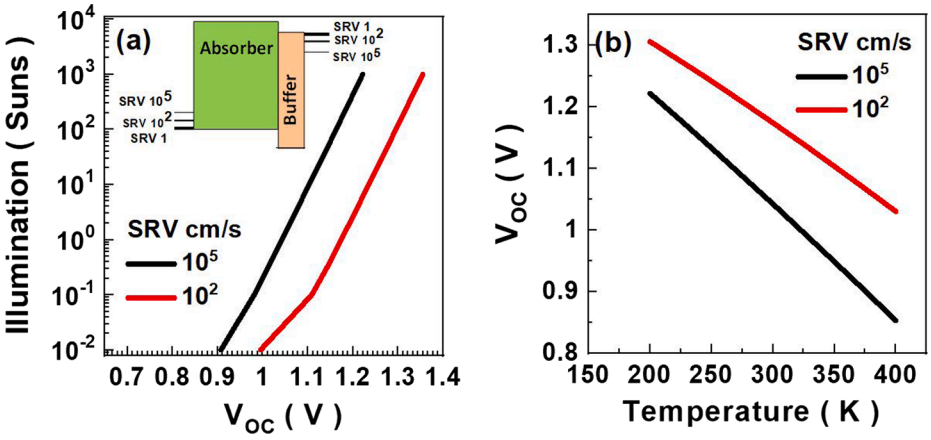

Fig. 7. (a) The V_{OC}-illumination plot for surface recombination velocities, (SRV). The V_{OC} increases linearly with illumination intensities for various values of SRV. High SRV lowers the V_{OC} output. The inset shows the schematic of the band diagram plot for depicting the various SRV values in the device. (b) The V_{OC} temperature plot shows V_{OC} linearly varies with temperature. The slope of the curve decreases with higher surface recombination velocity. SRV is varied in the range from 10^5 cm/s to 10^2 cm/s.

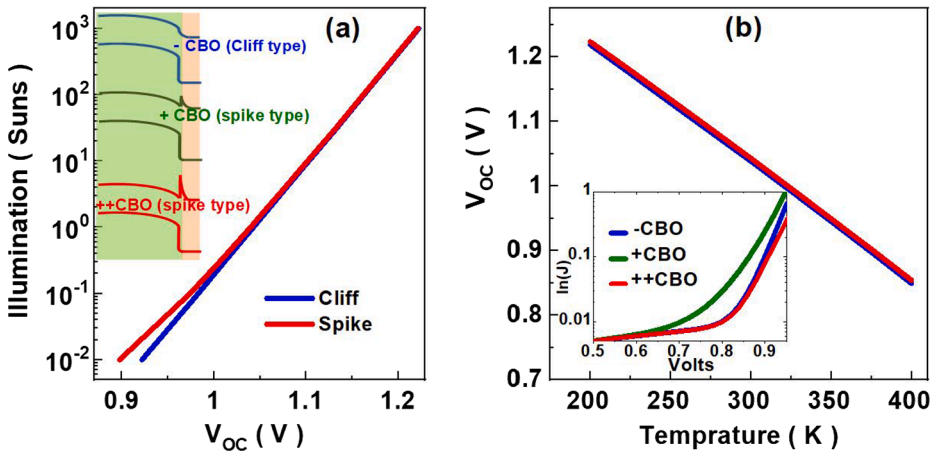

Fig. 8. (a) The V_{OC}-illumination plot for various CBO offset values. Inset shows the schematic of the band diagram for the negative, small positive and large positive conduction band offsets values. (b) V_{OC} as a function of temperature for various band offset values. Inset shows the simulated dark V-ln(J) curve for the different scenarios of band offsets. Higher current flows for slightly positive conduction band offset.

result in higher V_{OC} than higher SRV values. The slope of V_{OC} curves increases for higher SRV values and a downward shift is observed as seen in Fig. 7(b). It is to be noted that for 20% efficient device which will have a relatively superior device and material quality, SRV variation still causes an increment in V_{OC} values. The combined temperature and illumination plots show the linear variation of V_{OC} which present a distinct feature, different from that of the bulk defect, contact barrier, resistance, and hole mobility.

3.6. Impact of conduction band offset

The conduction band offset (CBO) in thin-film solar cell occur due to mismatch of electron affinity in a different layer of heterojunction. CBO is given by the difference of conduction band, E_C values of absorber and buffer layer. The schematic of CBO for cliff and spike type is shown in the inset of Fig. 8(a). Cliff type CBO has a lower efficiency than the spike type alignments. The slight spike is optimum alignments for optimum efficiency and minimum interfacial recombination. V_{OC} dependence on illumination is linear for cliff type CBO. The V_{OC} saturates moderately at a lower intensity for spike type CBO as shown in Fig. 8(a). The barrier at the interface $\varnothing_b^p$ effect V_{OC} as (Rau and Schock, 1999)

$$V_{oc} = \frac{\varnothing_b^p}{q} - \frac{KT}{q}\ln\frac{qS_pN_V}{J_{sc}} \tag{17}$$

where S_p is the interface recombination velocity for holes. The temperature dependence of V_{OC} is linear for different CBO alignments as shown in Fig. 8(b). The dark J-V curve is plotted for various conduction band offset (CBO) in the inset of Fig. 8(b). The current flow in the dark is higher for small spike type CBO as shown in the inset Fig. For both cliff type and highly positive spike, the current in dark is lower.

4. Conclusion

The bulk defect density in the absorber cause V_{OC} saturation in low illumination and at high temperature as observed in V_{OC} illumination and temperature plots. Rear contact barrier cause V_{OC} saturation at high illumination intensity and low temperatures in V_{OC} illumination and temperature plots. The shunt resistance causes V_{OC} saturation at low illumination with no impact on temperature dependences. Hole mobility causes moderate V_{OC} in high illumination intensity region and no impact on temperature plots. SRV causes a constant shift in V_{OC} values under illumination and temperature plots. Spike type CBO causes moderate saturation in low illumination whereas the cliff CBO does not give any such features. The combined illumination and temperature plots could reveal the presence and identify the bulk defect, contact barrier, resistance, hole mobility, SRV and CBO presence in the device. Table 2 summarizes the observation and feature observed in V_{OC} illumination and temperature plots for various defect conditions. We have simulated individual impact of a single defect at a time and observed the feature on V_{OC}-illumination and V_{OC}-temperature plot. A combined effect of two and more defects at a time and their impact on V_{OC} illumination and temperature plots and on other parameters (FF, J_{SC}) will be dealt in future work.

Table 2
Summary of impact on V_{OC}-illumination and V_{OC}-temperature plots caused by various defects. (for detail see text).

	V_{OC}-illumination		V_{OC}-temperature	
	Low illumination	High illumination	Low temperatures	High temperatures
Bulk Defect	V_{OC} decrease for high defect density	No impact	No impact	V_{OC} decrease for high defect density
Back contact barrier	No impact	V_{OC} saturates for high barrier	V_{OC} saturates for high barrier	No impact
Resistance	V_{OC} decrease for low shunt resistance	No impact	No impact	No impact
Hole mobility	No impact	V_{OC} saturates for low Hole mobility	No impact	No impact
SRV	V_{OC} level shift	V_{OC} level shift	V_{OC} level shift	V_{OC} level shift

Declaration of Competing Interest

The authors declare that they have no known competing financial interests or personal relationships that could have appeared to influence the work reported in this paper.

Acknowledgement

The author would like to heartily thank Professor Marc Burgelman, Department of Electronics and Information Systems, the University of Gent for providing the SCAPS software package.

References

Altındal, S., Kanbur, H., Yıldız, D.E., Parlak, M., 2007. Current conduction mechanism in Al/p-Si Schottky barrier diodes with native insulator layer at low temperatures. Appl. Surf. Sci. 253, 5056–5061.

Burgelman, M., Nollet, P., Degrave, S., 2000. Modelling polycrystalline semiconductor solar cells. Thin Solid Films 361–362, 527–532.

Chen, Q., McKeon, B.S., Zhang, S.Y., Zhang, F., Hu, C., Gfroerer, T.H., Wanlass, M.W., Smith, D.J., Zhang, Y., 2021. Impact of individual structural defects in GaAs solar cells: a correlative and in operando investigation of signatures, structures, and effects. Adv. Opt. Mater. 9, 2001487.

Das, B., Liu, Z., Aguilera, I., Rau, U., Kirchartz, T., 2020, Defect tolerant device geometries. arXiv:2008.13684.

Decock, K., Khelifi, S., Buecheler, S., Pianezzi, F., Tiwari, A.N., Burgelman, M., 2011. Defect distributions in thin film solar cells deduced from admittance measurements under different bias voltages. J. Appl. Phys. 110, 063722.

Elumalai, N.K., Uddin, A., 2016. Open circuit voltage of organic solar cells: an in-depth review. Energy Environ. Sci. 9, 391–410.

Green, M., 1982. Accuracy of analytical expressions for solar cell fill factors. Solar Cells 7 (3), 337–340. https://doi.org/10.1016/0379-6787(82)90057-6.

Green, M.A., Blakers, A.W., Zhao, J., Milne, A.M., Wang, A., Dai, X., 1990. Characterization of 23 -percent efficient silicon solar cells. IEEE Trans. Electron Devices 37, 331.

Gunawan, O., Gokmen, T., Mitzi, D.B., 2014. Suns-V_{OC} characteristics of high performance kesterite solar cells. J. Appl. Phys. 116, 084504.

Gunawan, O., Todorov, T.K., Mitzi, D.B., 2010. Loss mechanisms in hydrazine-processed $Cu_2ZnSn(Se, S)_4$ solar cells. Appl. Phys. Lett. 97 (23), 233506.

https://www.greentechmedia.com/articles/read/first-solar-hits-record-22-1-conversion-efficiency-for-cdte-solar-cell.

Islam, M.T., Thakur, A.K., 2020. Two stage modelling of solar photovoltaic cells based on Sb_2S_3 absorber with three distinct buffer combinations. Sol. Energy 202, 304–315.

Kumar, A., Thakur, A.D., 2018a. Role of contact work function, back surface field, and conduction band offset in Cu_2ZnSnS_4 solar cell. Jpn. J. Appl. Phys. 57, 08RC05.

Kumar, A., Thakur, A.D., 2018b. Design issues for optimum solar cell configuration. AIP Conf. Proc. 1953, 050022.

Kumar, A., Thakur, A.D., 2018c. The simulation of CZTS solar cell for performance improvement. AIP Conf. Proc. 1953, 050009.

Kumar, A., Thakur, A.D., 2018d. Improvement of efficiency in CZTSSe solar cell by using back surface field. Conf. Ser.: Mater. Sci. Eng. 360, 012027.

Kumar, A., Ranjan, P., 2018. Investigating absence of optimal photovoltaics response in CZTS solar cell. AIP Conf. Proc. 1953, 050024.

Kumar, A., Thakur, A.D., 2019. Comprehensive loss modeling in Cu_2ZnSnS_4 solar cells. Curr. Appl. Phys. 19, 1111–1119.

Kumar, A., Ranjan, P., 2020. Impact of light soaking on absorber and buffer layer in thin film solar cells. Appl. Phys. A 126, 397.

Kumar, A., 2021a. Impact of selenium composition variation in CZTS solar cell. Optik. 166421.

Kumar, A., 2021b. Numerical modelling of ion-migration caused hysteresis in perovskite solar cells. Opt. Quant. Electron.

Kaienburg, P., Krückemeier, L., Lübke, D., Nelson, J., Rau, U., Kirchartz, T., 2020. How solar cell efficiency is governed by the αμτ product. Phys. Rev. Res. 2, 023109.

Krysztopa, A., Igalson, M., Gütay, L., Larsen, J.K., Aida, Y., 2013. Defect level signatures in $CuInSe_2$ by photocurrent and capacitance spectroscopy. Thin Solid Films 535, 366–370.

Kaushal, P., Chand, S., Osvald, J., 2012. Current–voltage characteristics of Schottky diode simulated using semiconductor device equations. J. Electron. 100 (5), 686–698.

Luque, A., Hegedus, S., 2003. Handbook of Photovoltaics Science and Engineering. John Wiley and sons Ltd., Page no, p. 109.

Meher, S.R., Balakrishnan, L., Alex, Z.C., 2016. Analysis of Cu_2ZnSnS_4/CdS based photovoltaic cell: a numerical simulation approach. Superlattices Microstruct. 100, 703–722.

Metzger, W.K., Grover, S., Lu, D., 2019. Exceeding 20% efficiency with in situ group V doping in polycrystalline CdTe solar cells. Nat. Energy 4, 837–845.

Pan, J., Gloeckler, M., Sites, J.R., 2006. Hole current impedance and electron current enhancement by back-contact barriers in CdTe thin film solar cells. J. Appl. Phys. 100, 124505.

Rau, U., Schock, H., 1999. Electronic properties of Cu(In, Ga)Se2 heterojunction solar cells–recent achievements, current understanding, and future challenges. Appl. Phys. A 69, 131–147.

Reenen, S.V., Kemerink, M., Snaith, H.J., 2015. Modeling anomalous hysteresis in Perovskite solar cells. J. Phys. Chem. Lett. 6 (19), 3808–3814.

SCAPS Manual, Marc Burgelman, Koen Decock, Alex Niemegeers, Johan Verschraegen, Stefaan Degrave, Version: 18 may 2020.

Sadanand, A., Dwivedi, D.K., 2019. Theoretical investigation on enhancement of output performance of CZTSSe based solar cell. Solar Energy 193, 442–451.

Singh, P., Ravindra, N.M., 2012. Temperature dependence of solar cell performance—an analysis. Sol. Energy Mater. Sol. Cells 101, 36–45.

Sproul, A.B., 1994. Dimensionless solution of the equation describing the effect of surface recombination on carrier decay in semiconductors. J. Appl. Phys. 76, 2851.

Tress, W., Yavari, M., Domanski, K., Yadav, P., Niesen, B., Baena, J.P.C., Hagfeldt, A., Graetzel, M., 2018. Interpretation and evolution of open-circuit voltage, recombination, ideality factor and subgap defect states during reversible light-soaking and irreversible degradation of perovskite solar cells. Energy Environ. Sci. 11, 151–165.

Wang, J., Jariwala, S., Sinha, I., Jen, A.K.Y., Ginger, D.S., 2019. Reducing surface recombination velocities at the electrical contacts will improve perovskite photovoltaics. ACS Energy Lett. 4 (1), 222–227.

Würfel, U., Neher, D., Spies, A., Albrecht, S., 2015. Impact of charge transport on current–voltage characteristics and power-conversion efficiency of organic solar cells. Nat. Commun. 6, 6951.